Generation of Melt Streamline Patterns from Lithosphere Thickness Irregularities: An exploration using finite element methods

Undergraduate Honors Thesis

University of New Mexico Physics and Astronomy department

Rodrigo Osuna Orozco

Mentor: Prof. M. Roy

April 23rd, 2011

Abstract

Processes of melt generation and migration occurring at the lithosphere-asthenosphere interface in intra-plate regions (i.e., regions far from plate boundaries) have not received much attention by the geophysics community. We focus specifically on how variations in lithosphere thickness (undulations or roughness at the lithosphere-asthenosphere boundary) might control the transport of melt rising through the plate. We investigated the flow of a viscous fluid into a deformable porous matrix through the use of finite element methods. Such methods were implemented using the software named ELMER which is an Open Source Finite Element Software for Multiphysical Problems (http://www.csc.fi/english/pages/elmer). We present a series of simulations that constitute a first-order approximation to melt-migration at intra-plate settings where irregularities in the lithosphere thickness are purported to occur, e.g., a region of thicker lithosphere under the Colorado Plateau in the western US. The formation of dynamic pressure gradients due to flow of the asthenosphere around protrusions in the lithosphere present a consistent pattern with low dynamic pressures at the upwind side of the protrusion and high dynamic pressures at the downwind side of the protrusion. Such pressure gradients can cause melt to accumulate at low-pressure regions and flow away from high-pressure regions, controlled by the geometry of the lithosphere-asthenosphere boundary. Our simulations provide a first-order explanation for the observed lack of magmatic activity on the plateau and for the pattern of magmatic encroachment observed around certain margins of the Colorado plateau. This rather simple mechanism presented here might be more generally applicable in a number of settings and could be an important factor controlling the large scale distribution of melt at the Earth's surface.

Table of Contents

1. Introduction and Background

Melt generation and segregation are fundamental processes in the formation of the Earth's lithosphere[1] (Spiegelman et. al. 2007), which nonetheless are not well-understood. The process of melt segregation (motion of melt through a deformable matrix) has been typically modeled using the theory of two-phase flows; such theory incorporates "a set of conservation laws for mass, momentum and energy with phenomenological laws for fluxes of mass and heat" (McKenzie, 1984; Spiegelman, 1993; Rudge et. al. 2011). Moreover the problem can be modeled as the flow of a "low-viscosity fluid in a viscously deformable, permeable matrix" (Spiegelman 1993), where the low-viscosity fluid represents melt and the surrounding matrix represents rocks in either the asthenosphere or the lithosphere. Melt segregation is defined here as motion of the melt that is independent of the motion of the permeable matrix.

Two-phase flow is a well-studied problem and may include a number of processes that allow interaction between the melt and the matrix, namely, phase changes, chemical reactions, and time-dependent physical properties. The starting point for these models is the so-called "McKenzie Equations", which provide a fundamental framework for modeling magma migration (McKenzie, 1984). In this formulation, appropriate for geophysical flows within the Earth, it is assumed that the porosity and melt-fraction are equal (no voids exist). The equations are:

---

[1] The lithosphere (or "plate") is the mechanically strong, outer part of the Earth; it includes the crust and uppermost mantle and is a region where heat is transferred primarily by conduction; the asthenosphere is the flowing mantle beneath the lithosphere, where the dominant mode of heat transfer is convection.

(1)
$$\frac{\partial \rho_f \phi}{\partial t} + \nabla \cdot \left[\rho_f \phi\, \mathbf{v} \right] = \Gamma$$

(2)
$$\frac{\partial \rho_s (1-\phi)}{\partial t} + \nabla \cdot \left[\rho_s (1-\phi)\mathbf{V} \right] = -\Gamma$$

(3)
$$\phi(\mathbf{v} - \mathbf{V}) = -\frac{K}{\mu}[\nabla P - \rho_f \mathbf{g}]$$

(4)
$$\nabla P = \nabla \cdot (\mu[\nabla \mathbf{V} + \nabla \mathbf{V}^T]) + \nabla\left[\left(\zeta - \frac{2}{3}\mu\right)\nabla \cdot \mathbf{V}\right] + \bar{\rho}\mathbf{g}$$

Here the first two equations arise from conservation of mass for the fluid and solid phases respectively. And we allow mass transfer through phase change by the term Γ which is the crystallization rate (rate of mass transfer from solid to liquid). The third equation is a generalization of Darcy's law[2]; this governs the separation of melt from solid. Finally equation four is conservation of momentum for the solid matrix; note that this form of the conservation of momentum is derived by modeling the solid matrix as a compressible, inertia-free viscous fluid[3] (Spiegelman et al. 2007). Moreover, the solid pressure is divided into three components, namely $P=P_l+P+P^*$. Here P_l is the lithostatic pressure given by $\rho_s g z$ for constant solid density, P is proportional to the divergence of the solid velocity field (when flow is incompressible, $P=0$) and P^*, which contains all

---

[2] Darcy's law (which incidentally is not a law) defines the pressure gradient in a porous media to be a linear function of the velocity difference between solid and fluid phases. As noted by A. Cemal Eringen it may only strictly hold for inviscid fluids, and so in our case it is only a linear approximation (Eringen, 2003).
[3] Notice that we talk of a solid matrix and a melt but we model both as fluids, although of vastly differing viscosities (e.g. the solid matrix has a viscosity 20 orders of magnitude greater than that of the melt). Hence, it is possible to apply the concepts of fluid mechanics to the whole system.

other contributions to pressure (e.g., due to viscous shear), is called the dynamic pressure (Spiegelman et. al. 2007).

The variables are defined as follows:

Table 1: Physical Parameters for two Phase Flow		
Variable	Meaning	Range of values used
Φ	porosity	φ <<1 (low porosity limit)
ρ_s	Fluid density	2800 kg/m^3
ρ_f	Solid density	3300 kg/m^3
V	Fluid velocity field	10^{-9}-2.4*10^{-7} m/s
V	Solid velocity field	1.6^{-9} m/s – 0 m/s
	rate of mass transfer from solid to liquid	0 (no melting)
K	permeability	10^{-15} -10^{-12} m^2
M	melt viscosity	1 Pa-s
P	Fluid pressure	3.24^9-4.29^{10} Pa-s
G	Acceleration due to gravity	9.82 m/s^2
H	Solid shear viscosity	10^{18}-10^{25} Pa-s
Z	Solid bulk viscosity	Incompressible matrix
$\bar{\rho}$	$\bar{\rho} = \rho_f \phi + \rho_s(1 - \phi)$: mean density of the two phase system.	Low porosity limit, hence About 3300 kg/m^3

Based on Spiegelman et al., 2007 and McKenzie, 1984

In general two-phase flow refers to the situation where two phases of a substance coexist in a flow (such as in decompression melting and rising magma at a mid-oceanic ridge). There exist several analytical solutions to simple two-phase flow problems, specifically the case where the porosity (Φ), solid bulk viscosity ( ) and shear viscosity ( ) are constant and there is no melting (=0). In this case, the motion of the solid is that of an incompressible fluid and the only pressure-gradients in the system are gradients arising from viscous shear (first term in r.h.s. of Eqn. 4) and buoyancy (third term in r.h.s. of Eqn. 4). This set of assumptions was used to determine the trajectory of melt as it rises at a mid-ocean ridge where the separation of two plates is modeled as asymmetric corner-flow problem (Figure 1; Spiegelman 1993).
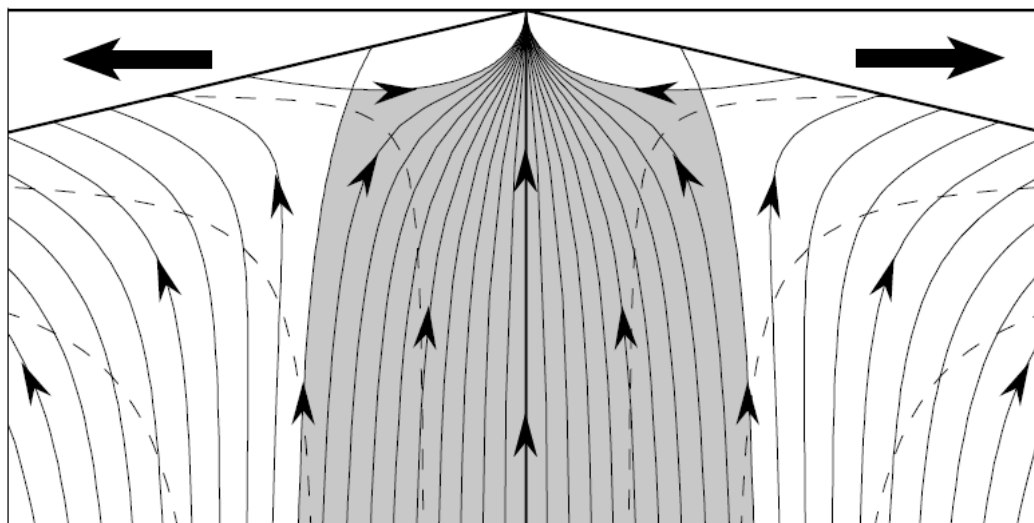
Figure 1: Example of an analytical solution for melt segregation. Melt and solid flow fields for the special case of constant porosity, constant viscosity. Taken from (Spiegelman et. al 2007). Solid flow (dashed lines) is given by corner flow solution (Batchelor, 2000) and the melt stream function (solid lines) are calculated from Eqn 3. The melt flows (solid lines) independently of the solid in this case.

Our goal is to understand the implications of a similar two-phase flow problem in the case where melt segregation occurs at the edges of a region of thicker lithosphere. As a first-order approach, we follow from Spiegelman (1993) and assume that there is no melting, constant porosity, and that the incompressible flow of the solid will generate dynamic pressure gradients due to shear that will drive segregation of melt from the solid (Eqn. 3). We start with an initial situation where melt is present in some uniform distribution (assumed constant, small porosity and constant permeability) in the asthenosphere as it flows past a step in the lithosphere. Melt segregation is predicted to be greatest in regions of high pressure-gradients, such as the margins of the thicker lithosphere. We will investigate whether regions with thicker lithosphere are therefore particularly prone to melt-extraction and magmatic activity at its margins. If so, then this would explain enigmatic observations such as the pattern of Cenozoic magmatic activity

surrounding the (thicker) Colorado Plateau region of the western US but a lack of magmatic activity within it (Figure 2). A primary target of this project is to explain the pronounced asymmetry in the pattern of melt-infiltration at the various margins of the Colorado Plateau. The purple arrow in Figure 2a shows the direction of relative motion of the North American plate relative to the mantle beneath it (Silver and Holt, 2002). In a reference frame stationary with respect to the Colorado Plateau, we would therefore expect the mantle to flow from SW to NE, although variations in lithosphere thickness along the way would locally disturb this flow. The patterns of magmatic activity show highest rates of encroachment on the SW (or "upwind") side of the plateau and no discernible encroachment on the NE (or "downwind" side of the plateau). In this project we explore how variations in the geometry of the lithosphere-asthenosphere boundary may be controlling the observed magmatic patterns.

A series of geophysical observations support the characterization of the Colorado Plateau as a region with a lithospheric thickness above that of the surrounding Great Basin. Findings by Sheehan et. al (1997) and also those by Zandt et al. (1995) based on seismic observations indicate a greater lithosphere thickness for the Colorado Plateau than for the surrounding Great Basin. Moreover, although the patterns of magmatism have been explained by a variety of factors (such as preexisting lithospheric weaknesses, e.g. Crow et al. 2011), the idea of an anomaly in the lithosphere thickness and shape below the Colorado plateau is commonly found in the literature (see figure 3).
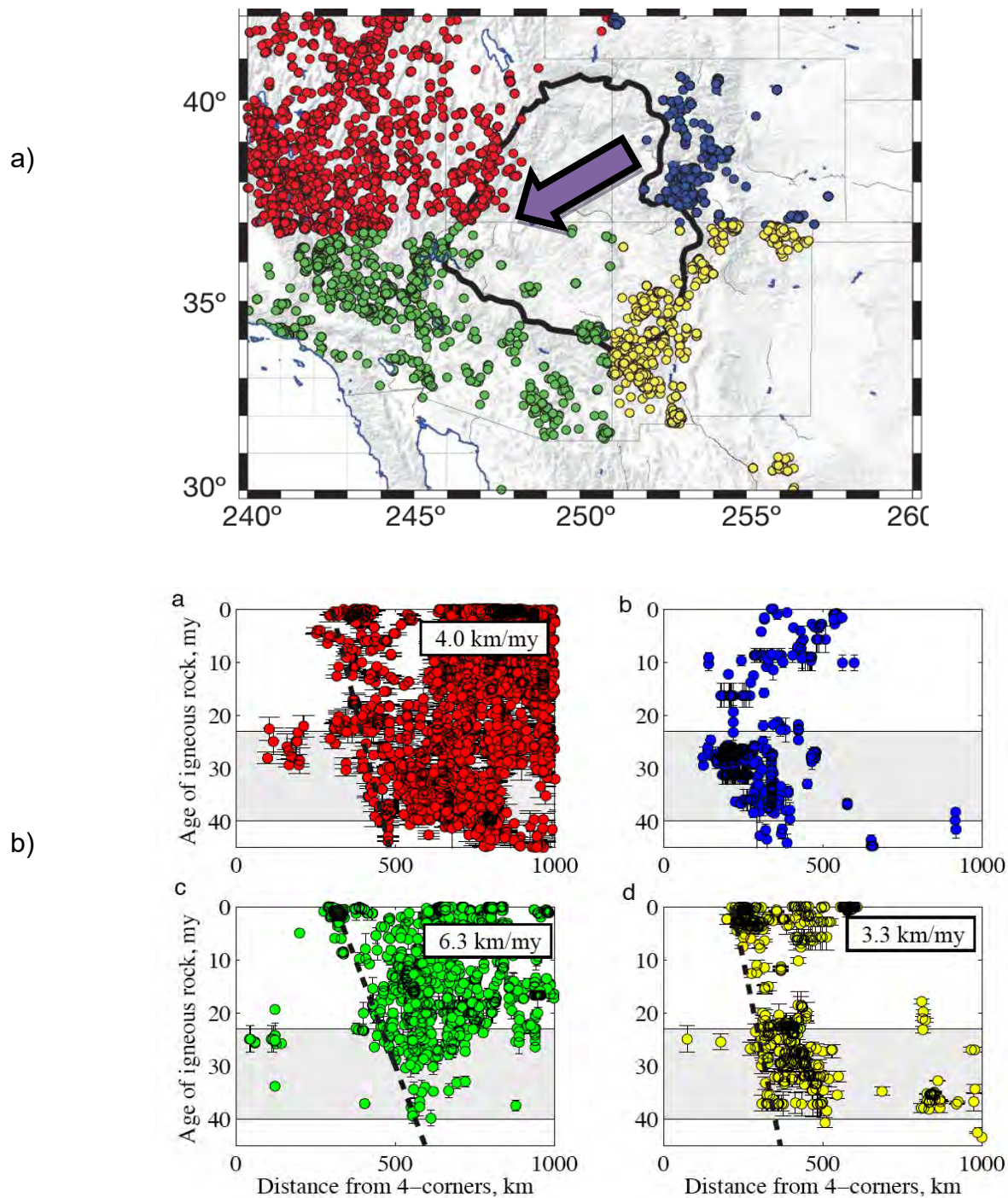
Figure 2: (a) From Roy et al. 2009. Cenozoic magmatic patterns in the western USA showing magmatic encroachment onto the Colorado Plateau. The arrow indicates the direction of the velocity of the Colorado plateau relative to the earth's core reference frame. (b) From Roy et al. 2009. Cenozoic magmatic patterns in the western USA showing magmatic encroachment onto the Colorado Plateau. a Distribution of Cenozoic volcanic rocks in the NAVDAT database with age uncertainties less than 5 Myr, color-coded by azimuth relative to the Four Corners point. Error bars indicate the minimum and maximum reported ages for a particular sample. Locations do not include structural reconstruction (e.g., in highly-extended regions), which is not a great source of error in undeformed regions such as the CP (outlined). b Igneous rock age as a function of distance from Four Corners, color-coded by quadrant as in (a). The dashed lines illustrate the encroachment of the onset of magmatism onto the plateau at the NW, SE, and SW margins at the rates indicated.
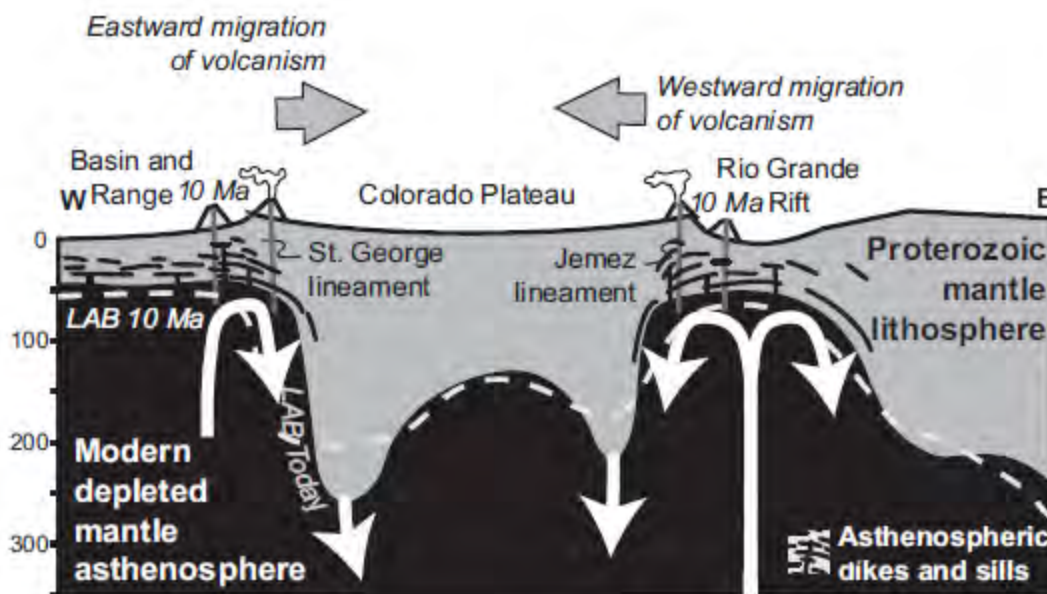
Figure 3: : Cartoon showing the Lithosphere Asthenosphere Boundary (LAB) at the present day, along with geologic evolution of the lithosphere beneath the Colorado Plateau. From Crow et al 2011.

Nonetheless the idea that the driving mechanism behind the asymmetric distribution of melt around the Colorado Plateau could be the pressure gradients generated by the flow of the asthenosphere around an irregular region of the lithosphere has not received much attention. Such an idea could easily extend to a variety to intraplate settings where there exists a characteristic roughness at the lithosphere asthenosphere boundary that controls the supply and migration of melt to the Earth's surface.

2. Model Setup and Assumptions

We can model the flow of magma below a protrusion in the lithosphere by defining two regions with differing mechanical properties. Although the problem is intrinsically three dimensional we develop a two dimensional model with the objective of finding the main effects of changing the geometry and mechanical properties of both materials (lithosphere and asthenosphere). Clearly treating the problem in the full three dimensions increases the computational demand of the simulations considerably. Moreover we assume that both layers have homogeneous density and viscosity.

On geologic timescales (> 10^4 years) both the lithosphere and the asthenosphere below it can be considered fluids of very high viscosity (above 10^{18} Pa-s), with the lithosphere having a greater viscosity than the asthenosphere. As outlined above, we assume that the porosity (ϕ), solid bulk viscosity ( ) and shear viscosity ( ) are constant and there is no melting (=0). In this case, the motion of the fluids representing the lithosphere and the asthenosphere is incompressible. All of these assumptions enable the use of the incompressible Navier-Stokes equation for solid flow. Moreover these assumptions allow us to get the relative motion of the melt and solid by equation 3 with P = $_s$gz+P*.

Thus we define a 1000m by 1000km square region with an obstacle at the top as our model domain (Figure 4). We assume that the top boundary is at a depth of 100km right at the average depth of the lithosphere-asthenosphere boundary. Moreover we establish periodic boundary conditions at the left and right edges of our box; this means that the values for pressure and velocity on one end are the same as those at the

opposite end, a situation which is equivalent to having an infinite series of identical boxes lying side by side (in the horizontal direction). Such an assumption may be justified as we consider a region of the plate which is far from any mid ocean ridges or subduction zones. Furthermore in these simple models we utilize a local reference frame with rectangular coordinates even though a length of a thousand kilometers at a hundred kilometer depth on earth would span an arc of 9.13 degrees (where the radius of the earth at the crust surface is 6378.1 km).
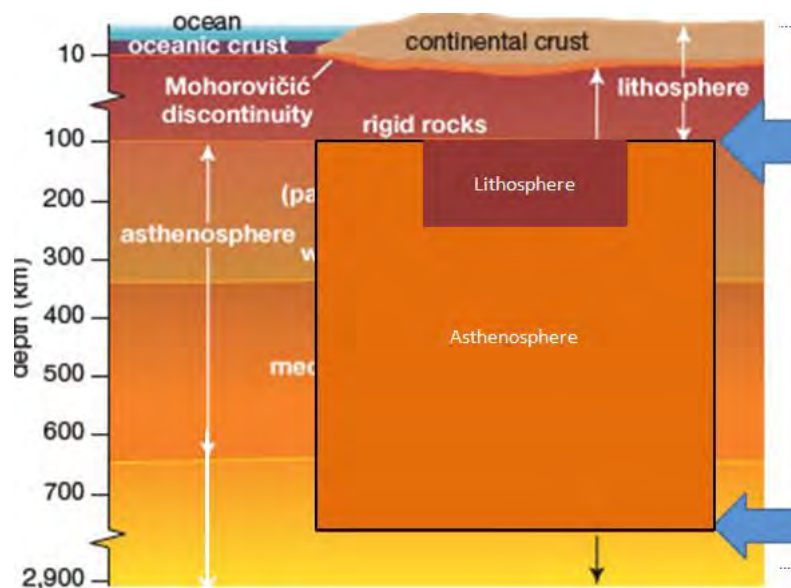

Figure 4: Cartoon of the basic geometry of our model (box with blue arrows showing the top and bottom boundaries of the model) and its position relative to the layers of the earth. Background taken from http://www.britannica.com/EBchecked/topic/343783/lithosphere.

Horizontal distances not to scale.

Finally, to generate dynamic pressure gradients we need the asthenosphere to flow in a prescribed manner. A simple way to achieve this is to start with Couette flow driven by the relative motion of two parallel planar walls. In our case, one of them is held stationary (the top boundary) and the other moves at a constant velocity (the bottom boundary, representing deeper mantle circulation). Under these assumptions, all velocities in our models are relative to a stationary top plate. With no-slip boundary

conditions one can easily find a steady state solution to the incompressible Navier Stokes equation:

(5)
$$\rho \frac{D\boldsymbol{u}}{Dt} = \rho\boldsymbol{g} - \nabla p + \mu\Delta\boldsymbol{u}$$

For plane Couette flow of an isoviscous fluid between planar walls we get:
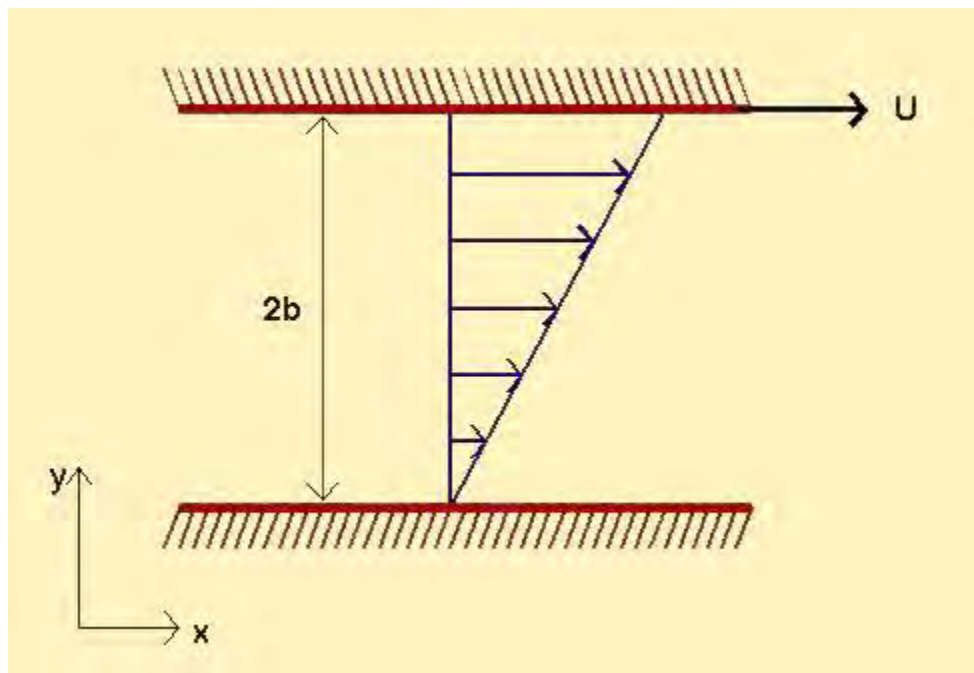
(6)
$$u = \frac{yU}{2b}$$

Figure 5: Plane Couette flow. From
http://www.student.math.uwaterloo.ca/~amat361/Fluid%20Mechanics/topics/laminar_flow.htm

Thus we see that we get a linear velocity profile. In all of our cases (which are not isoviscous) we could recover Couette flow by setting material properties inside the obstacle and outside of it to be equal (see figure 5). In our models we set the bottom boundary to move at a constant velocity of 5 cm/yr (~1.6e-9 ms^{-1}), comparable to rates

of motion of North America relative to the mantle beneath it as inferred from seismic anisotropy and GPS data (Silver and Holt, 2002).
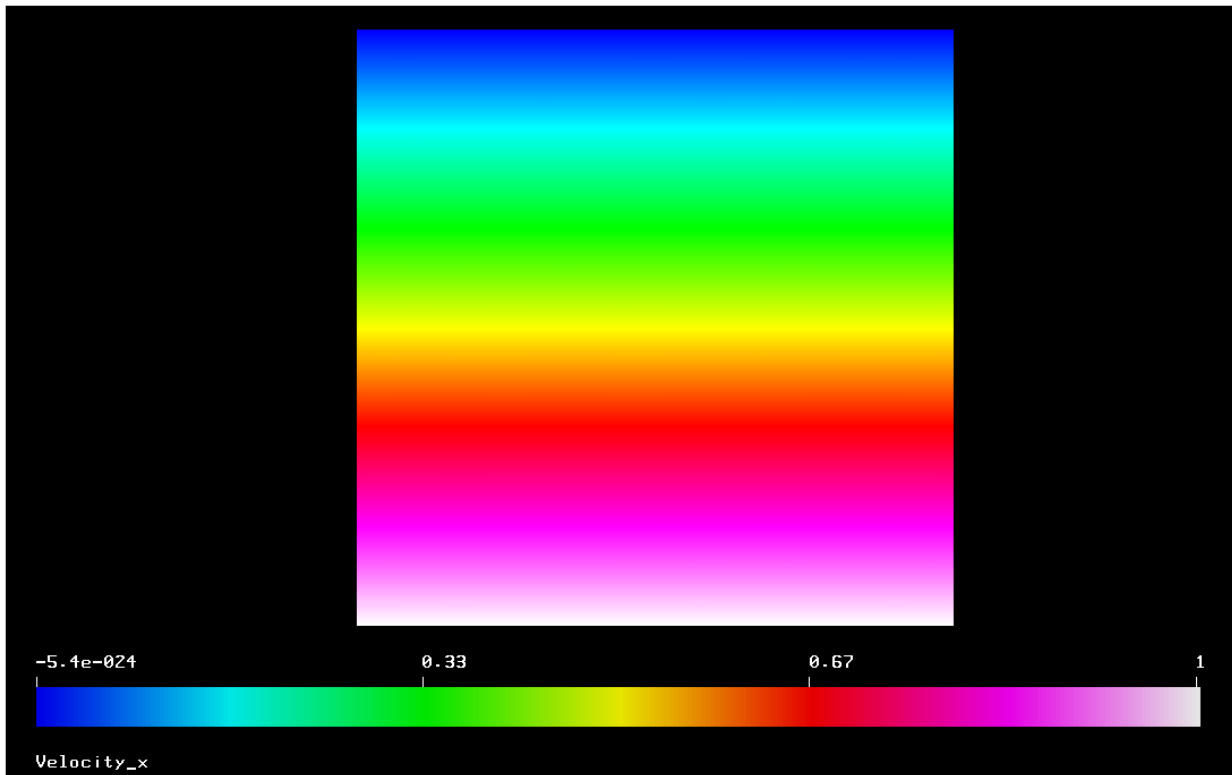

Figure 6: couette flow. We clearly observe the linear profile characteristic of couette flow.

2.1 Viscosity

We investigate the effects of increasing the "rigidity" of the asthenosphere underlying the lithospheric obstacle by varying the viscosity parameter (η) in both the lithosphere and the asthenosphere. For this purpose we define our lithosphere obstacle to be a semicircle in the middle of the box with a radius of 100 km; hence the whole diameter of our obstacle represents 20% of the box's length (see figure 6). Moreover we

define the densities of both bodies to be 3300 kgm^{-3} for all of our calculations. We performed calculations with viscosities ranging from 1e18 Pa-s to 1e25 Pa-s (see table above). These values for viscosities fall within the ranges estimated by Billen (2005) for Newtonian and non-Newtonian rheologies of the mantle.
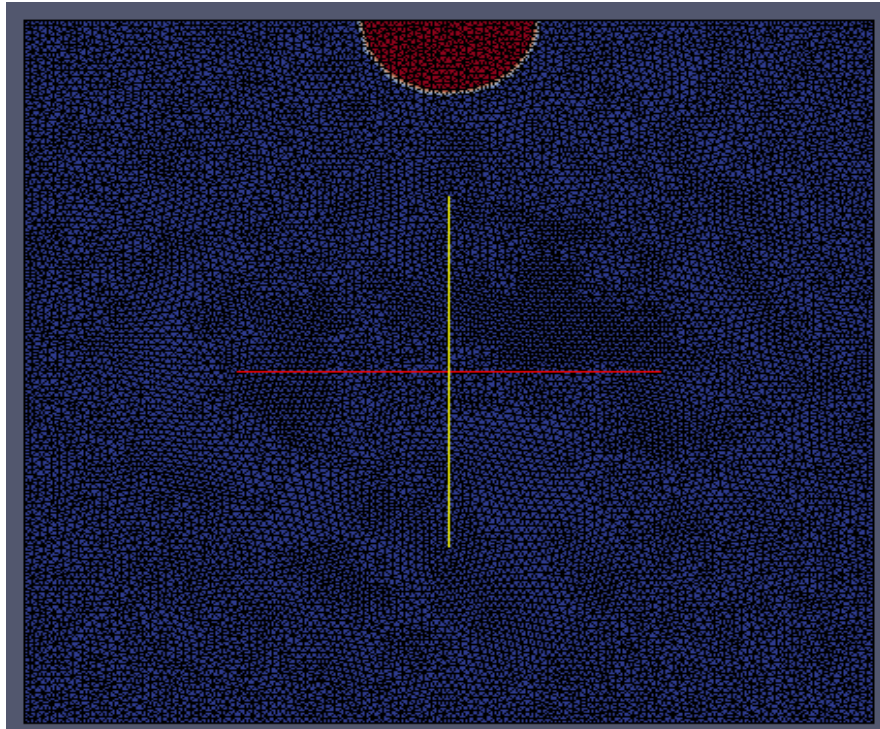

Figure 7: Example of the model geometry for the case of a fine mesh. The two bodies are colored by their viscosity (he region with the color gradient is just a result of an interpolation done by our imaging software). The mesh element-edges appear as black lines. Distance between nodes is about 10km. In this case, the obstacle (red) region is a factor 10X more viscous than the surrounding asthenosphere (blue).

The main feature observed is that the flow of the more viscous material generates dynamic pressures whose absolute values are symmetric about the obstacle and with opposite signs, with the low pressures in the upwind side and the high pressures in the downwind side (figure 8). Moreover we observe a linear relationship between the asthenosphere viscosity and the maximum dynamic pressure range, but no correlation between the lithosphere viscosity and the dynamic pressure range (figure 9).
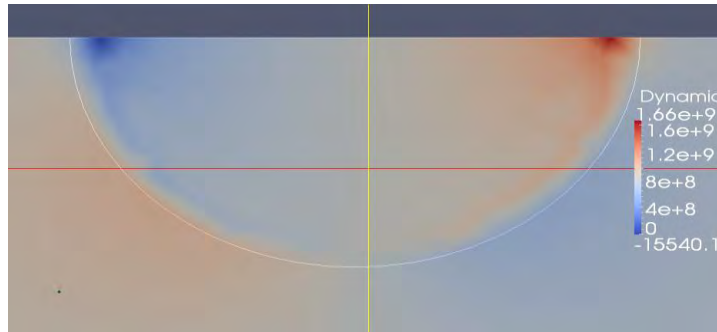
Figure 8: Dynamic pressure field across a hemispherical protrusion. Dynamic pressures are in Pa.

a)

b)

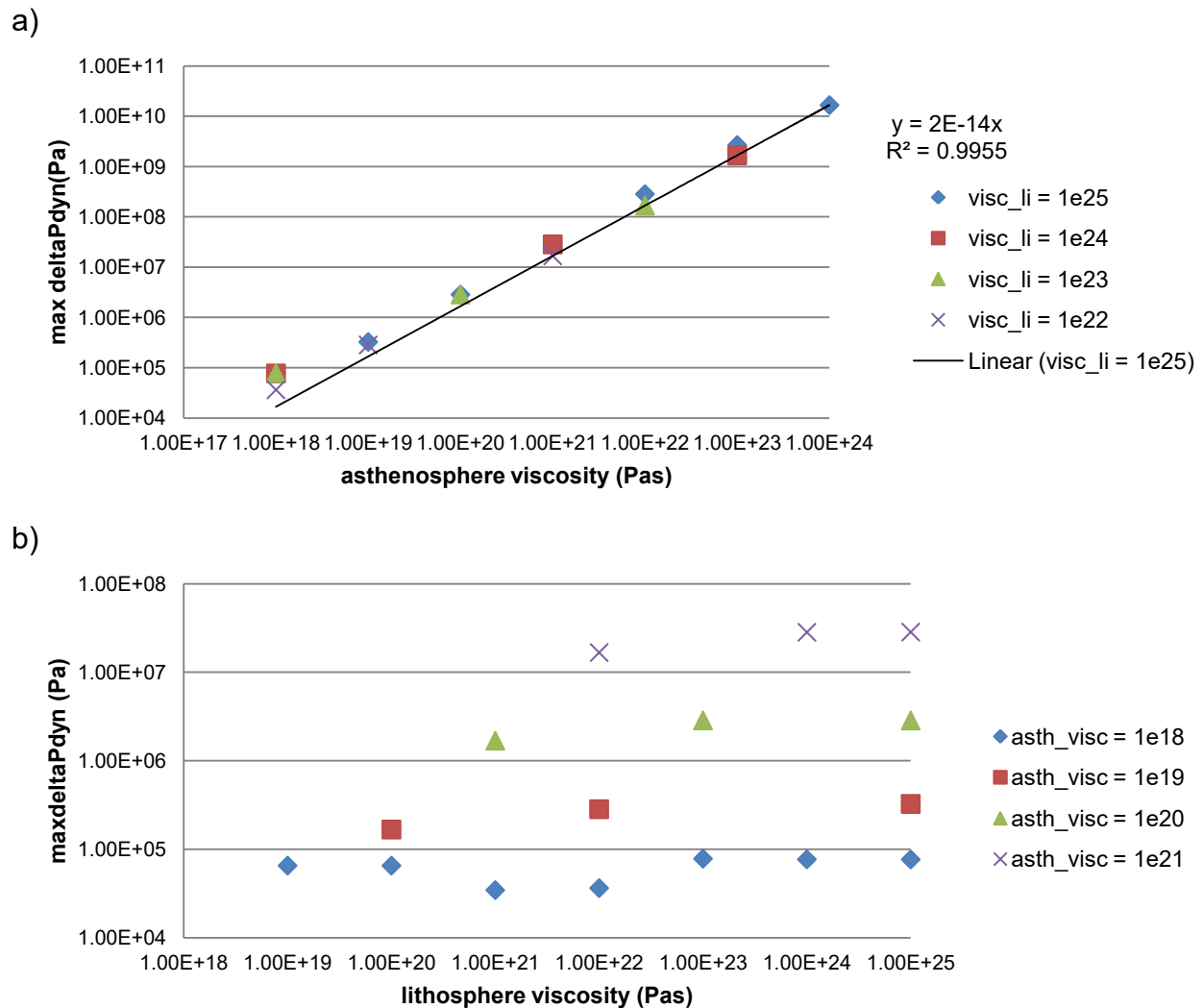Figure 9: Log-log plots of maximum dynamic pressure difference (in Pa) vs asthenosphere viscosity (in Pa-s); (a) and vs lithosphere viscosity (in Pa-s);(b). The fit in (a) was performed using the Microsoft Excel built-in fitting function.

Provided that the permeability is non-zero but constant, such dynamic pressure gradients will drive the flow of melt within the solid matrix (meaning both the lithosphere

and asthenosphere) according to equation 4 in such a way that melt is concentrated near the low-pressure, upwind border of the obstacle and driven away from the high-pressure downwind side of the obstacle (see figure 10). The upward movement of the melt is dominated by the buoyancy due to the difference in density between the two phases (we assume the melt to be less dense than the solid, as observed in laboratory experiments and also consistent with the observation of magma rising to the surface). Clearly the lower the density of the melt the greater it will be its tendency to rise, thus the greater the dynamic pressures required to have streamlines deviating from straight vertical paths.
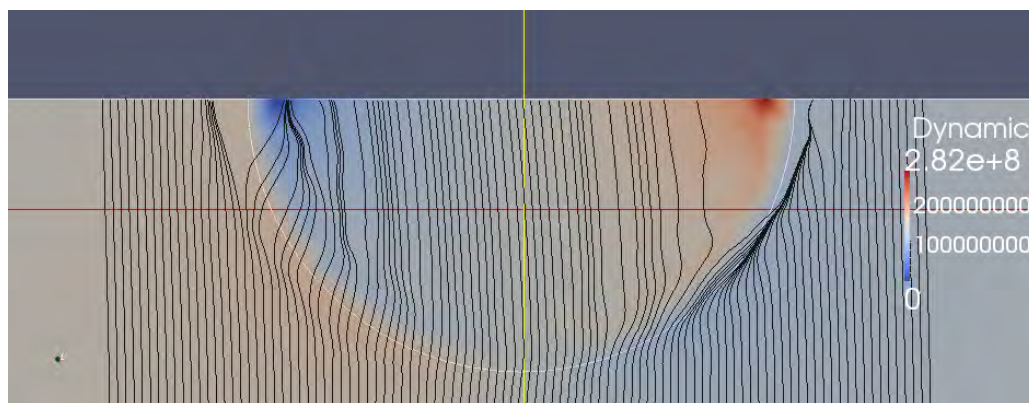
a)
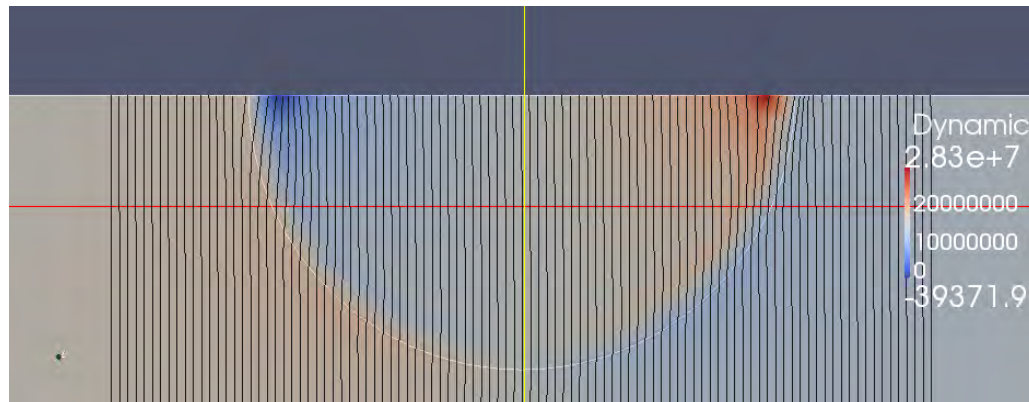
b)

Figure 10: Streamlines, for asthenosphere viscosity 1e21 Pa-s (a) and 1e22 Pa-s(b). In both cases the melt density is set to be 2800 kgm-3 and the lithosphere viscosity to be 1e25 Pa-s. Notice that raising the asthenosphere viscosity by an order of magnitude also. Dynamic pressures are in Pa.

2.2 Aspect Ratio

Besides changing the material properties of the two bodies it would be reasonable to expect that the streamlines followed by melt through the lithosphere and the asthenosphere might depend on the geometry of our protrusion in the lithosphere. Indeed the Navier-Stokes equation (equation 5) gives us reason to think that this is so since the derivatives of the pressure depend on the derivatives of the velocity (and we consider the low viscosity asthenosphere flowing around the lithosphere). An easy parameter to vary, considering our geometry above, is the radius of our semicircular obstacle (Figure 11). Thus we fixed the lithosphere viscosity to be 1e25 Pa-s and the asthenosphere viscosity to be 1e22 Pa-s, and we varied the radius of our obstacle to be between 50 km and 475 km (see figure 12 below). Typical dimensions of the Colorado Plateau region for example would imply an equivalent "radius" of about 300-400 km.
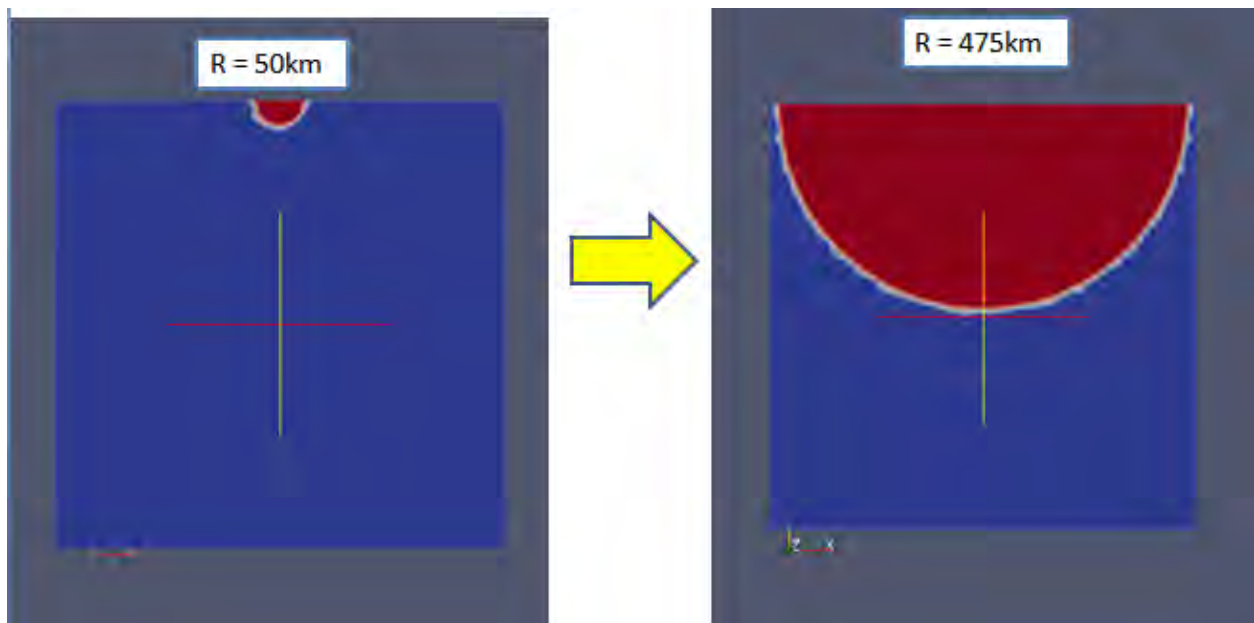
Figure 11: variation in radius. The bodies are colored by viscosity.
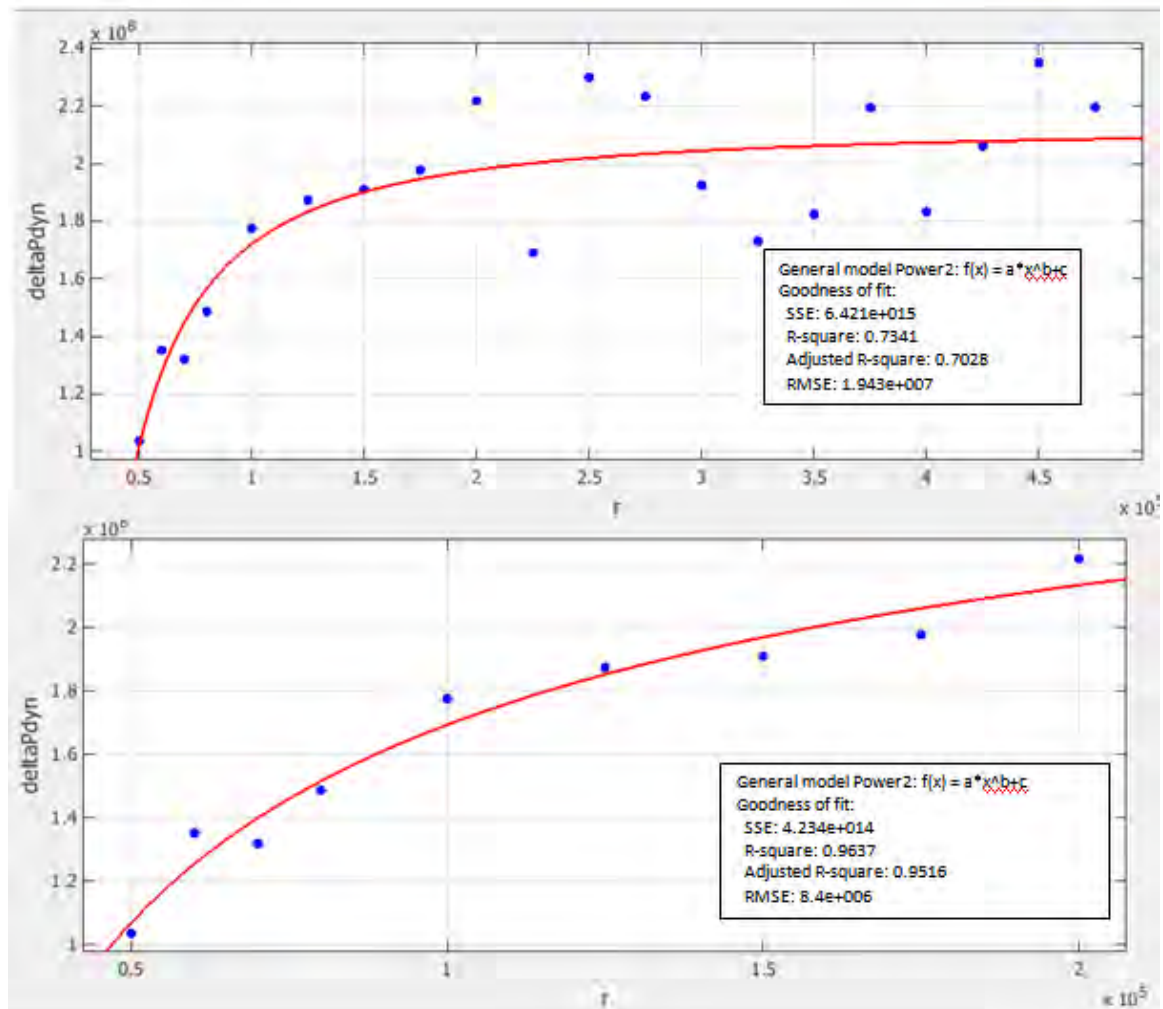
Figure 12: Plots of dynamic pressure range (Pa) and radius (m) of the semi-circular protrusion for radii ranging from 50km to 475km (up) and for radii ranging from 50km to 200km (down). The curve-fitting was done using MATLAB's curve-fitting toolbox.

We do not observe a clear correlation between the size of the obstacle and the dynamic pressure ranges. Nonetheless there seems to be a relation that breaks down after the size of the obstacle surpasses a certain threshold (in our case r = 2e5 m, or 20% of our box length). Below this threshold the dynamic pressure gradients seem to be a polynomial function of the protrusion's radius (see figure 12 below).

We can consider three main factors that will affect the dynamic pressure gradients while varying the radius of our obstacle: the length of the path of a particle flowing past the obstacle, the proximity of the obstacle to the left and right boundaries and the obstacle's proximity to the bottom. We would expect that a longer path around the obstacle would imply steeper velocity gradients and therefore increased shear stress, leading to higher dynamic pressures. Thus as we remain far from the edges we observe an increase in dynamic pressures with increasing obstacle size. Nonetheless, as we get closer to the boundaries the other contributions become noticeable. We would expect that getting closer to the bottom (which is driving the flow) would lead to greater velocity gradients at the lithosphere-asthenosphere boundary (although not necessarily a greater velocity at the boundary. We can think of this in terms of the Couette flow; in the case of Couette flow bringing the two plates closer together does not change the velocity at those plates but it does change the velocity gradient in the y direction (see equation 6). Moreover reducing the distance between the lithosphere-asthenosphere and the bottom of our box is somewhat analogous to reducing the distance between the two plates in the Couette flow. Thus we would expect a local increase in the velocity gradient as the obstacle gets closer to the bottom, which in turn would increase the shearing rate. On the other hand it is not all too clear what the effect of getting closer to the boundary will be, but we can conjecture that as the edges of the obstacle get closer to the edges of our box we are basically making a region of high pressure (at the downwind side of the obstacle) get closer to a region of low pressure (at the upwind side of the "image" obstacle implied by periodicity).

3. Sinusoidal Irregularities at the Lithosphere-Asthenosphere Boundary

In order to investigate the effects of obstacle size and inter-obstacle proximity more systematically, we consider a sinusoidally deformed lithosphere-asthenosphere boundary (see figure13). Thus we related the values of the wavelength and amplitude of a cosine function to the values for the dynamic pressure.
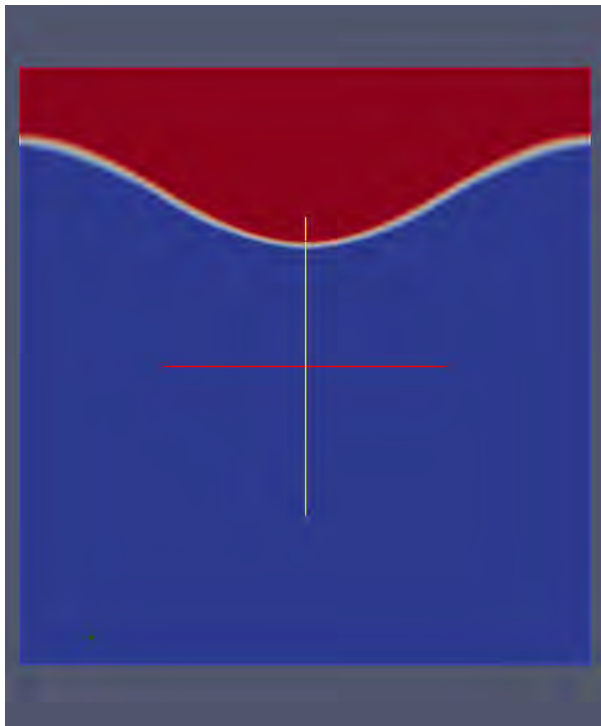

Figure 13: we consider the effect of a sinusoidally deformed lithosphere. Here the two layers are colored by viscosity (red is the high viscosity lithosphere and blue is the lower-viscosity asthenosphere).

Note that our models use quasi-sinusoidal boundaries rather than true sinusoids, for we defined a set of points in the mesh which were generated by a cosine function and then joined them using a smooth spline.

The distribution of low- and high-pressure regions described above for the case of the single obstacles is reproduced in this case for the local peaks (see figure 13). Moreover we observe that the dynamic pressure ranges increase linearly with increasing amplitude as well as with decreasing wavelength (see figure 14). Note that we consider only integer number of wavelengths in our domain since as stated above we enforce periodic boundary conditions at the edges, thus a non-integer number of wavelengths would lead to the geometry at the

boundary not being periodic. Moreover we observed an increase in the dynamic pressure ranges with decreasing distance of the boundary to the bottom of the domain (see figure 15). This is expected since, for incompressible flow, the asthenospheric fluid must be driven at high velocities through the gap between the obstacle and the bottom boundary.
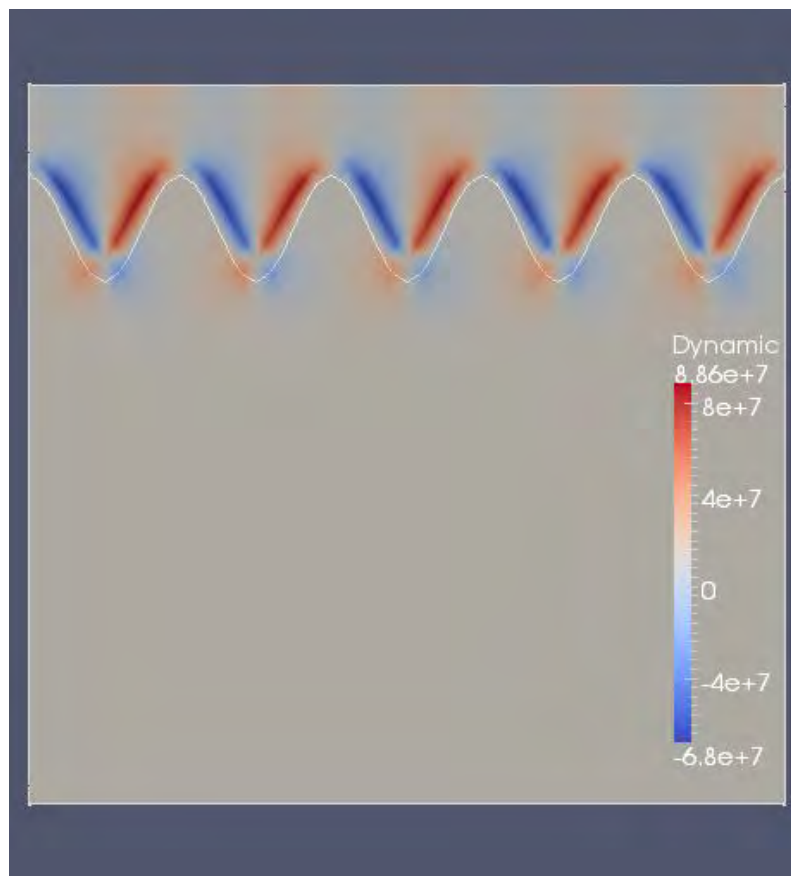
Figure 14: Dynamic pressure field for sinusoidally shaped boundary with wavelength equal to one fifth of our box's length. Dynamic pressures in Pa.

Thus we can characterize a roughness scale over which melt streamlines (with melt of a prescribed density) will deviate from vertical and thus create patterns of melt-focusing and lack of melt at the surface (see figure 16).
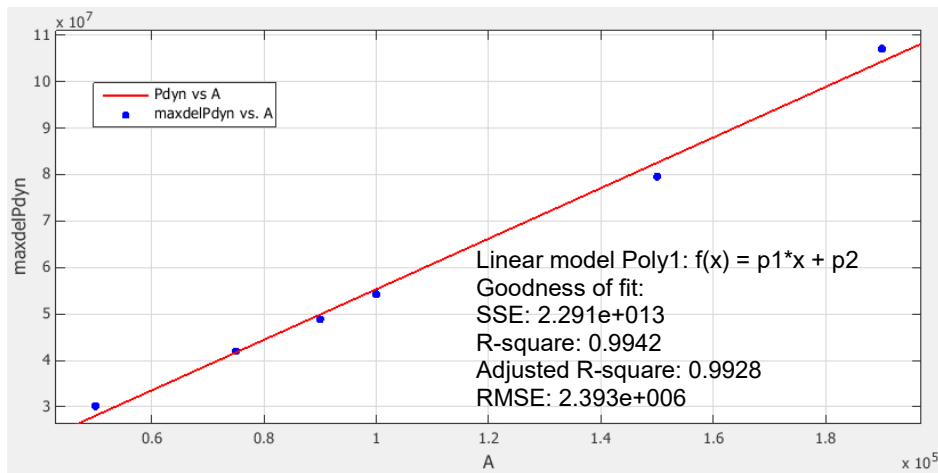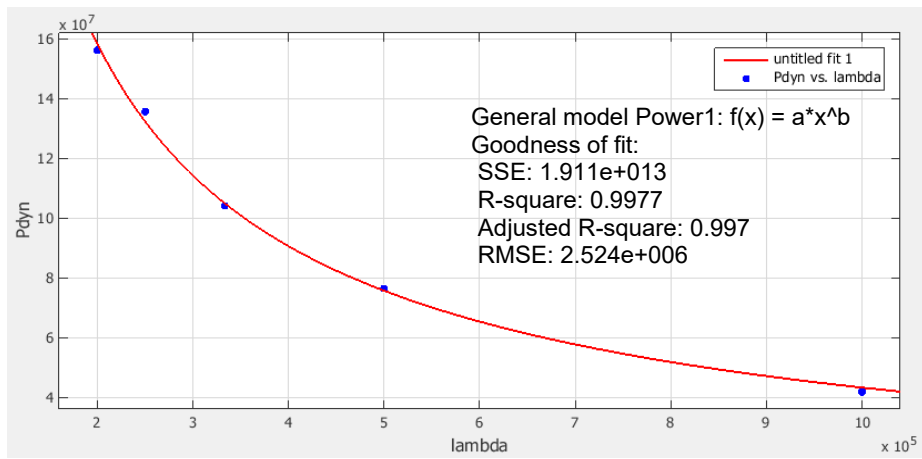
Figure 15: Plots of dynamic pressure range in Pa vs (a) Amplitude in meters (b) Wavelength in meters (c) Distance from the box bottom in meters.
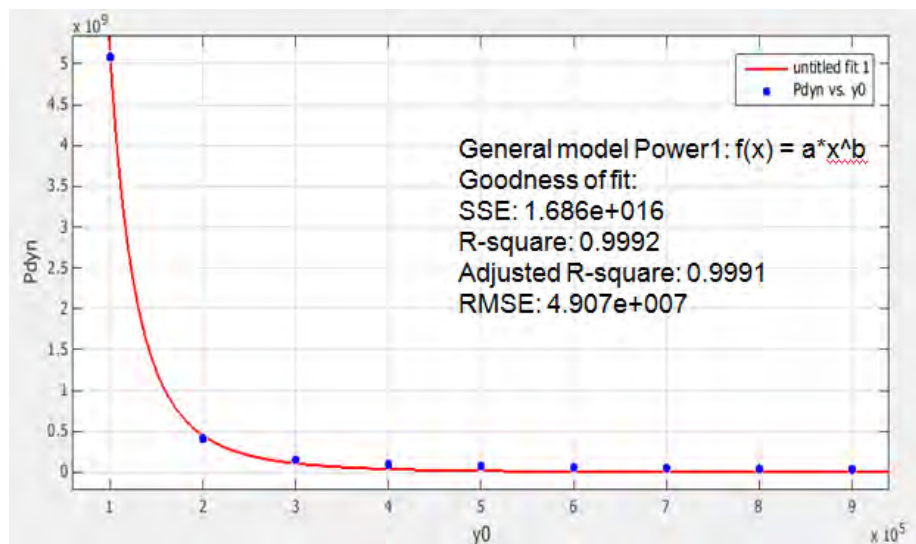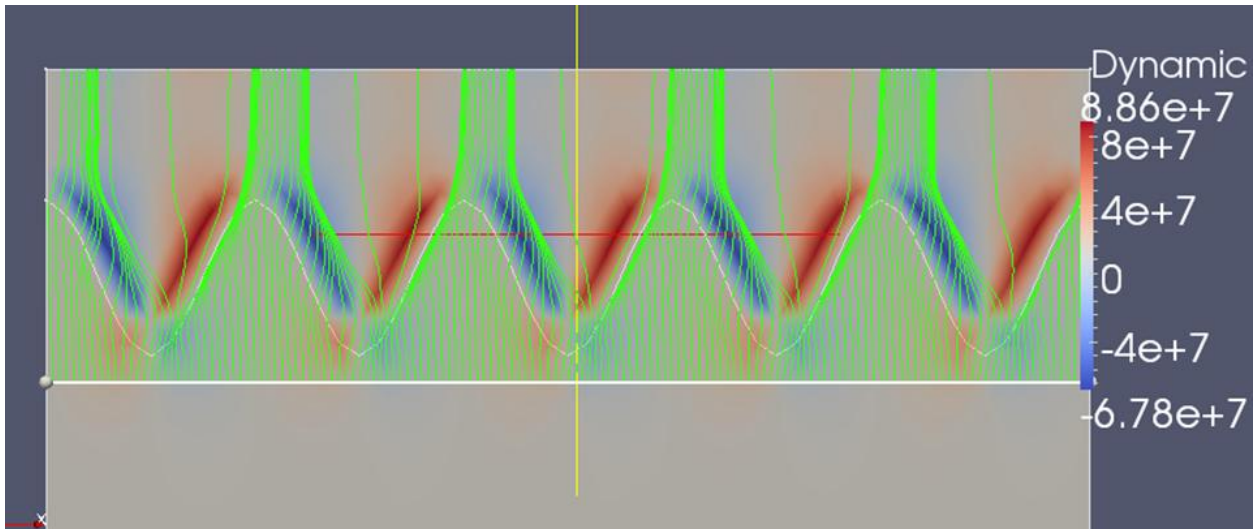
Figure 16: Periodic melt distribution pattern arising from a sinusoidal lithosphere asthenosphere boundary with wavelength equal to one fifth of the box length. Dynamic pressures are in Pa.

4. Conclusion

Our simulations show a consistent pattern of melt distribution that arises when a fluid of very high viscosity flows around an obstacle of higher viscosity. To the first order this pattern offers an explanation that links deep earth processes (i.e. processes occurring at the asthenosphere-lithosphere boundary) to observations of melt distribution at the surface. It is worthwhile noticing that such patterns arise for a wide range of viscosities, geometries and melt densities.

The results of our simulations are consistent with the observations of magmatic encroachment around the Colorado Plateau (Figure 2). Indeed the noticeable asymmetry of magmatic encroachment rates between the southwest and northeast margins could be explained by our results since the observed velocity of the Colorado plateau relative to the mantle is towards the southwest (figure 2a). Hence we can say that the asthenosphere is flowing to the northeast in the Colorado Plateau reference

frame. In such a frame we observe low magmatic encroachment in the downwind side of the Colorado Plateau (the northeast margin) and high magmatic encroachment rates in the upwind side (the southwest margin, see figure 2). Moreover we see that the margins that are closer to being parallel to the asthenosphere flow (northwest and southeast margins) show lower magmatic encroachment rates than the upwind side of the plateau.

5. Suggestions for further work

The work performed for this senior thesis focused on a toy model which used many simplifying assumptions. Further work should incorporate a series of extensions to this idea which bring the model closer to reality. Thus future work may include variable densities, viscosities and other mechanical parameters (such as bulk and shear modulus). Also it would be relevant to incorporate the effect of phase changes and having a compressible matrix (this will allow for a contribution from the divergence of the solid flow field to pressure-gradients; second term in Eqn. 4).

Furthermore this works naturally extends to the three dimensional case. Such an extension could consider performing the calculations in a spherical coordinate system and with boundary conditions which reflect the finiteness of the plates. Also more general large scale patterns of volcanism, for example at the Ring of Fire – the system of subduction zones at the edges of the Pacific Ocean, could be studied based on the principle that the distribution of melt at the boundary is determined by processes taking place at the lithosphere asthenosphere boundary.

6. Acknowledgements

References

Batchelor, G.K., An Introduction to Fluid Dynamics (Cambridge Mathematical Library), 2000.

Billen, M. I., Newtonian versus non-Newtonian upper mantle viscosity: Implications for subduction initiation. Geophysical Research, VOL. 32, L19304, 2005.

Crow, R. et al. Shrinking of the Colorado Plateau via lithospheric mantle erosion: Evidence from Nd and Sr isotopes and geochronology of Neogene basalts---Geology 2011

Eringen, A. C. Note On Darcy's Law. Journal of Applied Physics Volume 94, Number 2, 2003.

Hewitt, I.J., and Fowler, A.C. Melt Channelization in Ascending Mantle. Journal of Geophysical Research.   Vol. 114, B06210, 2009.

McKenzie, D, The generation and compaction of partially molten rock. *J. Petrol.*, 25:713–765,1984.

ParaView   User's   Guide   (v3.10)   –   found   at http://paraview.org/paraview/help/download/ParaView%20User%27s%20Guide%20v3.10.pdf

Roy, M., Holtzman, B. and Gaherty, J. Evaluating the roles of melt migration and mantle flow in lithospheric evolution: the Colorado Plateau as a geodynamic laboratory for EarthScope.

Roy, M., T.H. Jordan, and J. Pederson, Cenozoic magmatism and rock uplift of the Colorado Plateau by warming of chemically buoyant lithosphere, Nature 459, doi:10.1038/nature08052, 2009

Rudge, J.F., Bercovici, D., and Spiegelman, M. Disequilibrium Melting of a Two Phase Multicomponent Mantle. Geophys. J. Int. 184, 699-718, 2011.

Silver, P. G., and W. E. Holt (2002), The Mantle Flow Field Beneath Western North America, *Science*, *295,* 1054-1057.

Spiegelman, M., Flow in Deformable Porous Media . J. Fluid Mech, vol. 247, pp 17-38, 1993.

Spiegelman, M., Katz, R., and Simpson, G. An Introduction and Tutorial to the "McKenzie Equations" for Magma Migration. January 13, 2007.

Sheehan, A.F. et al Contrasting lithospheric structure between the Colorado Plateau and Great Basin: Initial results from Colorado Plateau – Great Basin PASSCAL experiment. – Geophysical research letters, vol.24, no.21, pages 2609-2612, November 1, 1997.

Zandt, G. et al. Crust and mantle structure across the Basin and Range- Colorado Plateau Boundary at 37°N latitude and implications for Cenozoic extensional mechanism. Journal of Geophysical Research, Vol. 100, NO. B6, PAGES 10,529-10,548, JUNE 10, 1995

Elmer Documentation at http://www.csc.fi/english/pages/elmer

Appendix A: Elmer Solvers and Implementation

Our simulations were performed using finite element methods implemented in the software package developed by the Finnish CSC - IT Center for Science. This is an multiplatform open source package which can be acquired at http://www.csc.fi/english/pages/elmer. This package utilizes a set of PDE solvers for solving Multiphysical problems. In this appendix we consider the most relevant solvers used for preparing this honors thesis as well as the solver input files (.sif) in which the description of the problem, solvers and methods are given. We used solvers for the Navier-Stokes and heat equations as well as a "flux-solver for computing pressure gradients.

The Elmer solver for the heat equation uses energy conservation as well as Fourier's law of conduction. This solver was coupled to the fluid flow solver by convection (Elmer Models Manual 2011). Initial conditions defined a higher initial temperature (1573 K) for the asthenosphere than for the lithosphere (1073 K). Also, the initial velocity field was zero for both bodies.

Elmer's flow solver was used to calculate the pressure and velocity fields using the incompressible Navier Stokes equation coupled to the heat equation by convection. Finally the flux solver was used to compute pressure gradients.

The values obtained are the result of transient calculations for time steps of the order of 10^5 years.

The results were visualized both in Paraview (after writing the results to VTK file format) and in the Elmer postprocessor module.

Sample SIF file

```
Header
  CHECK KEYWORDS Warn
  Mesh DB "." "."
  Include Path ""
  Results Directory ""
End

Simulation
  Max Output Level = 4
  Coordinate System = Cartesian
  Coordinate Mapping(3) = 1 2 3
  Simulation Type = Transient
  Steady State Max Iterations = 2
  Output Intervals = 1
  Timestepping Method = BDF
  BDF Order = 1
  Timestep intervals = 2
  Timestep Sizes = 3e12
  Solver Input File = case.sif
  Post File = case.ep
End

Constants
  Gravity(4) = 0 -1 0 9.82
  Stefan Boltzmann = 5.67e-08
  Permittivity of Vacuum = 8.8542e-12
  Boltzmann Constant = 1.3807e-23
  Unit Charge = 1.602e-19
End

Body 1
  Target Bodies(1) = 2
  Name = "Body 1"
  Equation = 1
  Material = 1
  Body Force = 1
  Initial condition = 1
End

Body 2
  Target Bodies(1) = 1
  Name = "Body 2"
  Equation = 1
  Material = 2
  Body Force = 1
  Initial condition = 2
End

Solver 3
```

```
  Equation = Flux and Gradient
  Flux Coefficient = 1
  Target Variable = Pressure
  Procedure = "FluxSolver" "FluxSolver"
  Enforce Positive Magnitude = True
  !Calculate Flux = True
  Calculate Grad = True
  Calculate Grad Magnitude = True
! Calculate Flux Magnitude = True
  Exec Solver = Always
  Stabilize = True
  Bubbles = False
  Lumped Mass Matrix = False
  Optimize Bandwidth = True
  Steady State Convergence Tolerance = 1.0e-5
  Nonlinear System Convergence Tolerance = 1.0e-8
  Nonlinear System Max Iterations = 20
  Nonlinear System Newton After Iterations = 3
  Nonlinear System Newton After Tolerance = 1.0e-3
  Nonlinear System Relaxation Factor = 1
  Linear System Solver = Iterative
  Linear System Iterative Method = BiCGStab
  Linear System Max Iterations = 500
  Linear System Convergence Tolerance = 1.0e-8
  Linear System Preconditioning = ILU0
  Linear System ILUT Tolerance = 1.0e-3
  Linear System Abort Not Converged = False
  Linear System Residual Output = 1
  Linear System Precondition Recompute = 1
End

Solver 1
  Equation = Navier-Stokes
  Procedure = "FlowSolve" "FlowSolver"
  Variable = Flow Solution[Velocity:2 Pressure:1]
  Exec Solver = Always
  Stabilize = True
  Bubbles = False
  Lumped Mass Matrix = False
  Optimize Bandwidth = True
  Steady State Convergence Tolerance = 1.0e-5
  Nonlinear System Convergence Tolerance = 1.0e-8
  Nonlinear System Max Iterations = 20
  Nonlinear System Newton After Iterations = 3
  Nonlinear System Newton After Tolerance = 1.0e-3
  Nonlinear System Relaxation Factor = 1
  Linear System Solver = Iterative
  Linear System Iterative Method = BiCGStab
  Linear System Max Iterations = 500
  Linear System Convergence Tolerance = 1.0e-8
  Linear System Preconditioning = ILU0
```

```
    Linear System ILUT Tolerance = 1.0e-3
    Linear System Abort Not Converged = False
    Linear System Residual Output = 1
    Linear System Precondition Recompute = 1
End

Solver 2
  Equation = Heat Equation
  Procedure = "HeatSolve" "HeatSolver"
  Variable = -dofs 1 Temperature
  Exec Solver = Always
  Stabilize = True
  Bubbles = False
  Lumped Mass Matrix = False
  Optimize Bandwidth = True
  Steady State Convergence Tolerance = 1.0e-5
  Nonlinear System Convergence Tolerance = 1.0e-8
  Nonlinear System Max Iterations = 20
  Nonlinear System Newton After Iterations = 3
  Nonlinear System Newton After Tolerance = 1.0e-3
  Nonlinear System Relaxation Factor = 1
  Linear System Solver = Iterative
  Linear System Iterative Method = BiCGStab
  Linear System Max Iterations = 500
  Linear System Convergence Tolerance = 1.0e-8
  Linear System Preconditioning = ILU0
  Linear System ILUT Tolerance = 1.0e-3
  Linear System Abort Not Converged = False
  Linear System Residual Output = 1
  Linear System Precondition Recompute = 1
End

Solver 4
  Exec Solver = String "after timestep"
  exec interval = 1
  Procedure = File "SaveData" "SaveMaterials"
  Parameter 1 = String "Density"
  Parameter 2 = String "Viscosity"
  Parameter 3 = String "Dynamic"
  Parameter 4 = String "Total_p"
End

Equation 1
  Name = "nav_stokes heat flux mesh"
  Active Solvers(4) = 3 1 2 4
End


Material 1
  Name = "lithosphere"
  Reference Temperature = 1573
```

```
   Viscosity = 1e25
   Heat expansion Coefficient = 2.5e-5
   Heat Conductivity = 3
   Heat Capacity = 1000
   Density = 3300
   Compressibility Model = Incompressible

   Total_p = Variable Pressure, Density
   Real MATC "2.00691e10+ tx(1)*9.82*100e3 + tx(0)"
   Dynamic = Variable Total_p, Density, Coordinate 2
   Real MATC "tx(0) + tx(1)*9.82*(tx(2)-1100e3)"

End

Material 2
   Name = "asthenosphere"
   Reference Temperature = 1573
   Viscosity = 1e22
   Heat expansion Coefficient = 2.5e-5
   Heat Conductivity = 3
   Heat Capacity = 1000
   Density = 3300
   Compressibility Model = Incompressible

   Total_p = Variable Pressure, Density
   Real MATC "2.00691e10+ tx(1)*9.82*100e3 + tx(0)"
   Dynamic = Variable Total_p, Density, Coordinate 2
   Real MATC "tx(0) + tx(1)*9.82*(tx(2)-1100e3)"

End

Body Force 1
   Name = "hydrostatic pressure"
   Hydrostatic pressure = True
End

Initial Condition 1
   Name = "InitialCondition 1"
   Velocity 2 = 0
   Velocity 1 = 0
   Temperature = 1073
   Velocity 3 = 0
End

Initial Condition 2
   Name = "InitialCondition 2"
   Velocity 2 = 0
   Velocity 1 = 0
   Temperature = 1573
   Velocity 3 = 0
End
```

```
Boundary Condition 1
  Target Boundaries(1) = 1
  Name = "inlet"
End

Boundary Condition 2
  Target Boundaries(1) = 2
  Name = "bottom move"
  Velocity 3 = 0
  Velocity 1 = 1.6e-9
  Velocity 2 = 0
  Temperature = 1573
End

Boundary Condition 3
  Target Boundaries(1) = 3
  Name = "outlet"
  Periodic BC Velocity 3 = True
  Periodic BC Pressure = True
  Periodic BC Velocity 1 = True
  Periodic BC = 1
  Periodic BC Velocity 2 = True
End


Boundary Condition 5
  Target Boundaries(1) = 4
  Name = "interphase"
  Temperature = 1573
End

Boundary Condition 6
  Target Boundaries(1) = 7
  Name = "dome top"
  Noslip wall BC = True
End


Solver 5 ! Set the correct solver number here.
        ! Usually you want to use the highest number so the results are saved at the end of a
timestep.
  Exec Solver = String "after timestep"
  exec interval = 1
  Equation = String "ResultOutput"
  Procedure = File "ResultOutputSolve" "ResultOutputSolver"
  Output File Name = String "paraver_cos_wave_5_A." !or any other output file name of your
choice
  Output Format = String "vtk"
  Vtk Format = Logical True
End
```

Appendix B: Mesh Generation and Visualization

We created all of our meshes using the program Gmsh (copyright (C) 1997-2011 by C. Geuzaine and J.-F. Remacle). This allows the creation of meshes with triangular elements based on the user definition of bodies and boundaries. Bodies are sets of nodes within the mesh to which a set of material parameters can be assigned. Gmsh generates meshes and writes them in the .msh format, which besides headings includes a list with the coordinates for each of the mesh nodes and a list with the relations between nodes that define the mesh elements.

Such files were converted to a set of files that served as an input into the elmer solver (thus generating four files). For this purpose the mesh generation and manipulation utility program ElmerGrid was used. Moreover Elmergrid allowed us to improve our meshes by its capability to get rid of superfluous nodes which are not used in any element.

Such meshes served as the input geometries for the elmer solver application through which we defined the attributes of the problem and obtained numerical solutions using robust algorithms. We employed the following solvers: heat equation solver, Navier-stokes equation solver and the flux-solver (see Appendix A on Elmer).

Finally the results were outputted to vtk files to be viewed and analyzed in the open source visualization application Paraview developed by Kitware, Sandia National Labs and CSimSoft. Calculation of melt velocity fields (relative to the solid matrix) were performed using the resulting pressures from the solution of the incompressible Navier

stokes equation, and Eqn. 3. The separation velocity field thus calculated was integrated in order to obtain melt streamlines relative to the solid.